DOI: 10.61782/fa.2025.0972

FORUM ACUSTICUM EURONOISE 2025

XAI BASED FREQUENCY-TIME FEATURE EXTRACTION AND DEVELOPMENT OF AN OPTIMAL EVALUATION METHOD FOR C-EPS

Junseo Park[1*] Hyeon-choel Jo[1] Inje Cho[1] Jaeyong Seo[1] Seongsik Yoo[1] Sangkyeong Lee[1]
Seungjae Bang[2] Jeongryeol Oh[2] Cholhawn Jeong[2] Sungzoon Cho[2]
[1] Hyundai Mobis, Yongin-si Gyeonggi-do Republic of Korea
[2] Big Data AI Center, Seoul University, Republic of Korea

ABSTRACT

The C-EPS (Column Type Electric Power Steering) system is a vehicle system that help smoother steering for the driver. When defects occurred in the components, interference noises may arise during steering, leading to driver discomfort. Conventional End-of-Line (EOL) testing, which detects defective C-EPS through order tracking at varying steering speeds, suffers from low detection rates due to boundary condition variations and low signal-to-noise ratios. Recently, many studies about anomaly detection have shown high detection rates, but these methods face challenges with unpredictable performance, vulnerability to small design changes, new types of interference noises and data imbalance.
This study aims to address these challenges by collecting defective C-EPS data for different types of interference noise phenomena and constructing an XAI (explainable AI) model to extract FTFM (Frequency-Time Feature Map) frequencies. Due to the inherent characteristics of real-world testing, ensuring the robustness of the model is challenging. Therefore, instead of directly using the model for defective C-EPS detection, a quantitative evaluation was conducted using the extracted FTFM. These FTFM incorporate noise and vibration characteristics, such as rotational components and resonance within mechanical systems, contributing not only to defect detection but also to potentially reducing the time required to resolve related issues.

Keywords: *c-eps, anomaly detection, nvh, xai, fft*

[*] ***Corresponding author***: *JunseoPark@mobis.com*

1. INTRODUCTION

EPS (Electric Power Steering) is a steering system in vehicles that assists the driver's steering using an electric motor [1]. When the driver turns the steering wheel, the system transmits the driver's input torque, angular velocity, and other physical information to the ECU (Electro Control Unit). The power generated by the motor is then passed through a reduction gear, providing the driver with an appropriate steering feel. It is classified into C-EPS, P-EPS (Pinion type Electric Power Steering), and to R-EPS (Rack Type Electric Power Steering) based on the reduction method (worm wheel & shaft, belt) and location. The mentioned EPS systems are appropriately selected according to the required rack force of the vehicle.
C-EPS is primarily used in relatively small vehicles due to its low permissible output. It is mounted on the steering column, which is in close to the driver's seat, making it relatively disadvantageous in terms of noise levels. The noise generated in C-EPS consists of operation noise, which occurs from the motor, reduction gear, and bearings during continuous steering wheel movement; knocking noise, which arises when the steering wheel is turned left and right; and rattle noise, which is caused by gear backlash and gap in the components when driving on rough road surfaces. This study focuses solely on the operation noise that may occur in C-EPS, especially on the interference noise.
Research on deep learning based anomaly detection is actively being conducted to detect anomalies or novel phenomena, such as interference noise, which do not occur in normal products at the EOL. Various studies have shown high defect detection rates by considering the effects of SNR and domain shifting on robust autoencoder-based models [2-5], generating data through NVH simulators to overcome the difficulty of obtaining sufficient data in real-world scenarios [6], and using data augmentation methods to increase the amount of data [7]. Although these methods show high defect detection rates, it is practically impossible

to replace EOL quality inspection equipment for the application of deep learning due to various reasons [8]. Additionally, due to the nature of the vehicle development cycle, designs often change before sufficient defective data is accumulated, making it difficult to trust the applied models. Focusing on these issues, this study proposes a method where the deep learning model does not directly classify defective products. Instead, it extracts FTFM through XAI, which serves as the basis for the model's defect classification. This approach can be applied to existing EOL equipment and can lead to the analysis of the causes of defects through signal post-processing.

2. MAIN NOISE SOURCES OF C-EPS

The noise of the C-EPS is primarily analyzed through order analysis [9]. The frequency range of the noise source can be calculated by multiplying the relative order with respect to the reference shaft by the rotational speed of the reference shaft as in Eqn. (1).

$$Frequency\ [Hz] = Order\ X\ \frac{Rotational\ speed\ of\ the\ reference\ shaft\ [RPM]}{60\ [sec]} \quad (1)$$

The main component of operation noise generated in C-EPS are as follows:

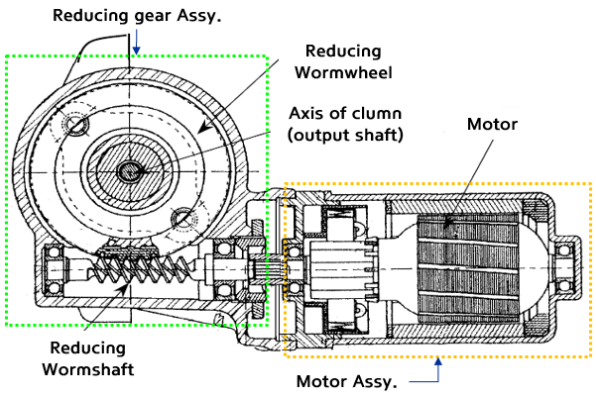

Figure 1. The concept of the C-EPS system.

2.1 Motor

The motor generates a magnetic field by switching the direction of the current through the stator windings. The rotor interacts with the stator's magnetic field and begins to rotate. The generated power then rotates the motor pulley, which, through the coupler, rotates the worm shaft. The noise from the motor can be broadly categorized into aerodynamic, mechanical, and electromagnetic noise. In the case of motors used in C-EPS systems, since they operate at low speeds, electromagnetic noise is dominant [10]. The order of motor noise, when calculated with respect to the motor shaft, is determined by the LCM (Least Common Multiple) of the pole & slots as in Eqn. (2).

$$Order_{Motor} = L.C.M.of\ pole\ \&\ slot \quad (2)$$

2.2 Reduction gear

Gear noise is caused by the repetitive contact of the teeth during the meshing process of the reduction gear (worm wheel and worm shaft), resulting in noise [11]. Gear noise is influenced by various factors, including transmission error, design (such as profile and lead), manufacturing methods, surface roughness, load due to gap between components and lubricating grease. The order of gear noise, when calculated with respect to the steering column, is determined by the number of teeth on the worm wheel as in Eqn. (3).

$$Order_{reduction\ gear} = N_{teeth,\ wormwheel} \quad (3)$$

2.3 Bearing

Bearings are used to reduce friction between components, providing better rotation, load support, and power transmission efficiency. Although they are not a primary source of noise under normal C-EPS operating conditions, they can produce perceptible noise if contaminated, lack lubrication, or damaged during manufacturing or transportation [12]. The fault frequencies of bearings include the Ball Pass Frequency Outer (BPFO), Ball Pass Frequency Inner (BPFI), Ball Spin Frequency (BSF), and the Fundamental Train Frequency (FTF). The above frequencies are determined based on bearing specifications such as N (the number of balls), α (the contact angle of the ball bearing), D (the diameter of the ball bearing), and P (the pitch diameter). The order of bearing fault noise, when calculated with respect to the Shaft with a bearing mounted, is determined as in Eqn. (4)-(7).

$$BPFO = \frac{N}{2} \times \left(1 - \frac{D}{P}\cos(\alpha)\right) \quad (4)$$

$$BPFI = \frac{N}{2} \times \left(1 + \frac{D}{P}\cos(\alpha)\right) \quad (5)$$

$$BSF = \frac{P}{D} \times \left[1 - \left(\frac{D}{P}\cos(\alpha)\right)^2\right] \quad (6)$$

$$FTF = \frac{1}{2} \times \left(1 - \frac{D}{P}\cos(\alpha)\right) \quad (7)$$

3. FREQUENCY-TIME FEATURE EXTRACTION

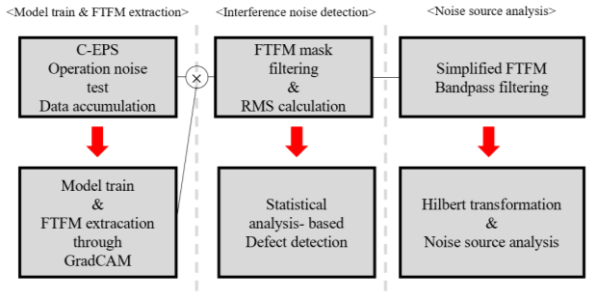

Figure 2. The overall process of extracting FTFM and noise source analysis

The process of extracting FTFM from the C-EPS is shown in Figure 2. Physical information during C-EPS operation was collected using microphone and accelerometers. These data were processed through appropriate signal processing steps to create an input shape suitable for the model train. The model was trained using the 2D shape STFT (Short-Time Fourier Transform) inputs to obtain model with high accuracy. By utilizing XAI (eXplainable AI), FTFM were obtained that serve as the basis for distinguishing between normal and defective products. Additionally, the validity of the noise and vibration characteristics of FTFM will be verified through signal post-processing methods.

3.1 Data accumulation

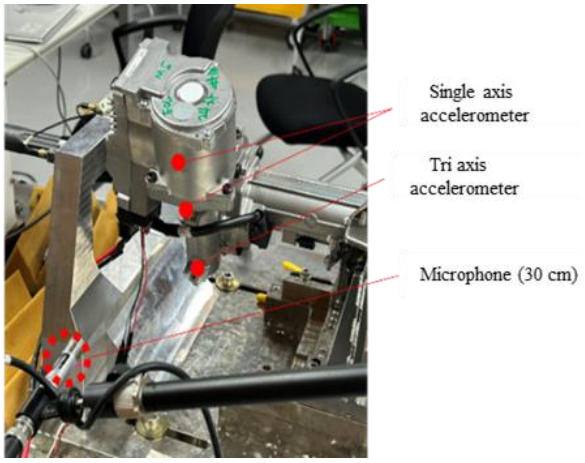

Figure 3. System level operation noise test for C-EPS

The operation noise test of C-EPS conducted using a system-level test setup that simulated conditions similar to vehicle-level test. Microphones were used to measure the noise levels. While there were no issues in the current test setup, which was conducted in an anechoic chamber, noise measurement would be difficult on the EOL test. Therefore, accelerometers were attached to the motor, and both the upper and lower ends of the worm shaft as in Figure 3. To analyze the noise trend based on the driver's steering speed, the test was conducted using an accelerated steering method. The relative tilting amount between the worm shaft and the worm wheel differs depending on CW (Clock Wise) and CCW (Counter Clock Wise) steering; thus, measurements were conducted twice for each case. A total of 533 sound pressure & acceleration dataset were collected per sensor by replacing the component with defective ones identified during the EOL inspection. Each dataset was labeled based on the evaluator's subjective assessment as 'Normal' or as interference noise types 'A,' 'B,' and 'C'. Type 'A' noise occurred intermittently, type 'B' was perceived as periodic impact noise, and type 'C' was recognized as friction noise. Out of the total 533 dataset, 298 correspond to ‘Normal’, while 30, 107, and 98 data points were collected for interference noise types 'A,' 'B,' and 'C,' respectively. In actual testing, obtaining evaluation dataset for defective products is challenging, raising concerns about the model's robustness. However, in this study, a balanced dataset was secured, except for interference noise type 'A'.

3.2 Preprocessing

The collected time dataset was transformed into the frequency domain using STFT. The signal processing parameters used for this transformation are in Table 1.

Table 1. The signal processing parameters

Sampling Frequency	12800 Hz
Frequency resolution	10 Hz
Window	Hanning
Overlap	70 %

Typically, a smaller frequency resolution is used to obtain more detailed frequency information. However, when using for model training, an excessively small resolution may lead to significant asymmetry in the input shape, causing an imbalance in the FTFM extraction. Therefore, appropriate parameters were selected to avoid this issue. The preprocessed input data has a shape of (380, 641), corresponding to 380 along the time axis and 641 along the frequency axis.

3.3 Model train

Table 2. The validation accuracy for each sensor, ResNet18

Sensor	Validation accuracy [%]
Microphone	97.2
Motor	92.5
Worm shaft upper	94.4
Worm shaft lower	95.3

Due to the inherent limitations in securing a large dataset for operation noise test, ‘ResNet’ which features residual connections, was employed [13]. This model was chosen as CNN are known to outperform transformer model when trained on limited dataset [14]. Among them, to prevent overfitting and minimize information loss in the last convolution layer, which is used for FTFM extraction, the relatively lightweight model 'ResNet18' was chosen. In cases with limited dataset, accuracy can vary significantly depending on the data used for training. Therefore, k-fold cross-validation (k=5) was employed to assess potential biases introduced by the train data. The validation accuracy for each sensor of the model is in Table 2. Since the model is not directly used for defective C-EPS classification, improving validation accuracy was not the primary objective. However, to ensure the reliability of the model for frequency-time feature extraction, a validation accuracy of over 90% was targeted.

3.4 XAI

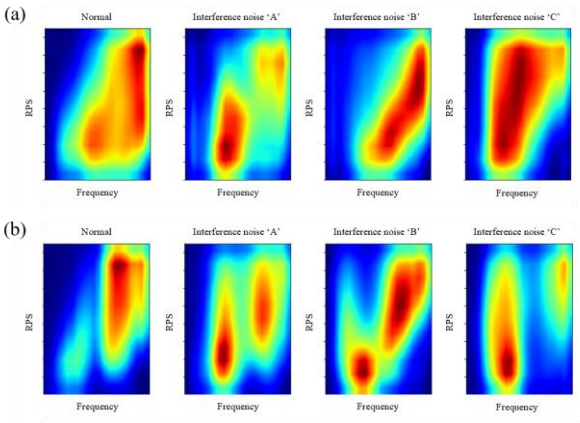

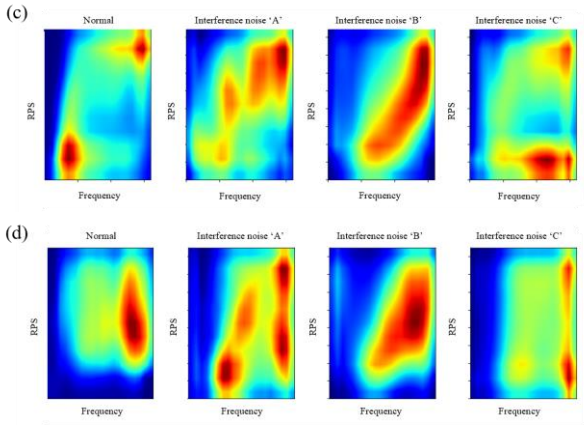

Figure 4. FTFM extraction ('Normal', interference noise types ‘A’, ‘B’, and ‘C’) of (a) microphone, accelerometers for (b) motor, (c) worm shaft upper and (d) worm shaft lower.

The FTFM of Normal and defective C-EPS were extracted from the trained model using Grad-CAM [15], one of the XAI techniques that can serve as a basis for decision-making as in Figure 4. In this study, other XAI techniques such as LIME (Local Interpretable Model-agnostic Explanation) [16] and SHAP (Shapley Additive explanation) [17] were not used, as they made it difficult to interpret the intuitive meaning of the feature frequencies and had longer computation times. Grad-CAM calculates the importance(weight) of the frequency-time features through a gradient approach, allowing for a visual representation of which parts of the STFT the model focused on when determining whether the test dataset is classified as ‘Normal’, interference noise types ‘A’, ‘B’ or ‘C’. Each data’s FTFM were averaged for each label. The extracted FTFM were standardized to a range of 0 to 1 to ensure consistency in scale. Seeing the results for interference noise type 'A', due to its intermittent occurrence, it makes hard to evaluator label the interference noise. The difficulty in clearly identifying the interference noise label continues to interpret the results challenging. However, for interference noise type 'B', the FTFM shows a diagonal pattern, like an order component, which confirms that the issue is related to a specific rotating part. In the case of interference noise type 'C’, identified as friction noise, a wide range band (especially 2~4 kHz) of frequencies is extracted as the frequency-time feature map. The frequency-time feature map of ‘Normal’ appears to reflect both order-related and wide range band characteristics, similar to those of 'B' and 'C,' to distinguish between ‘Normal’ and interference noise. Additionally, when

comparing the FTFMs of the microphone and accelerometers, a primary difference is that the accelerometer's FTFM give less importance to the nearby 3 kHz range compared to the microphone's FTFM. This can be explained by the interference of motor control-related frequencies [10], which hinder the identification of defective C-EPS. In summary, FTFM reveals that the model focuses on higher frequency regions compared to main orders of C-EPS.

4. RESULTS

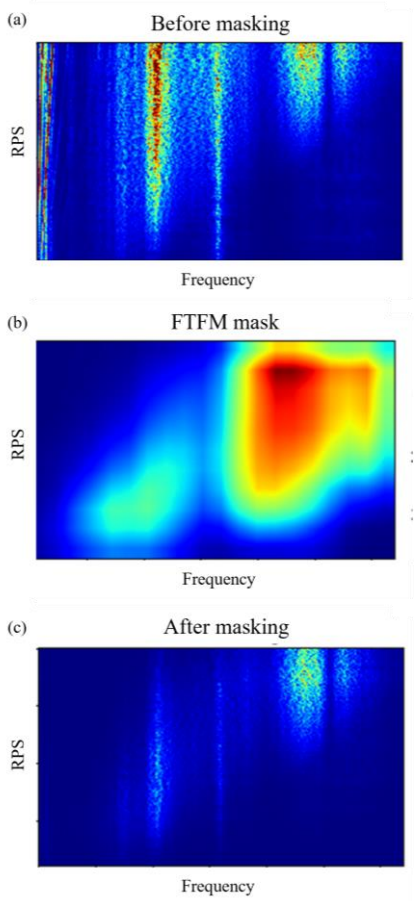

Figure 5. The process of frequency-time feature mask filtering, (a) operation noise STFT Before masking, (b) FTFM mask and (c) operation noise STFT After masking

The extracted FTFM was used as a filtering mask and multiplied with the input operation noise STFT dataset results to highlight the specific steering speed and frequency regions that the model considers essential for classification as shown in Figure 5. The masked STFT results were compared using the RMS (Root Mean Square) values. As shown in Figure 6, maximum(Q3+1.5*IQR) of 'Normal' C-EPS was selected as the threshold to evaluate the defect detection rate.

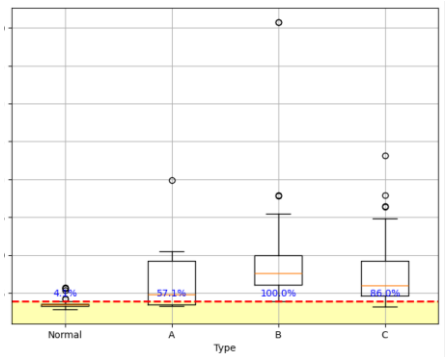

Figure 6. The example box plot of motor acceleration RMS values and defect detection rate (red dashed line, threshold)

The defect detection rate for each sensor is in Table 3. Compared to conventional analysis methods such as O/A(Overall) for observing general frequency trends and Order Analysis for identifying specific rotational components, the proposed approach demonstrates an improved defect detection rate. Notably, a higher detection rate was observed in the microphone and motor accelerometer. This indicates that a high validation accuracy of the model does not necessarily lead to an improvement in the defect detection rate based on mask filtered RMS values. Rather, it is assumed that the improvement in defect detection rate is influenced by the type and location of the sensors.

Table 3. Comparison of defect detection rates among O/A, Order, and FTFM analysis methods.

		Defect detection rate [%]		
Sensor	Analysis method	'A'	'B'	'C'
MIC	O/A	25.0	64.8	40.9
	Order	21.6	36.2	21.6
	FTFM	57.1	98	88
Motor acc	O/A	17.8	35.2	13.6
	Order	12.2	13.6	9.1
	FTFM	57.1	100	86
Worm shaft Upper Acc	O/A	24.4	72.7	29.5
	Order	12.2	14.8	10.2
	FTFM	35.7	90.0	74.0

Worm shaft Lower Acc	O/A	20.0	56.8	35.2
	Order	10.0	6.8	6.8
	FTFM	57.1	94.0.	86.0

4.1 Noise source analysis using the FTFM

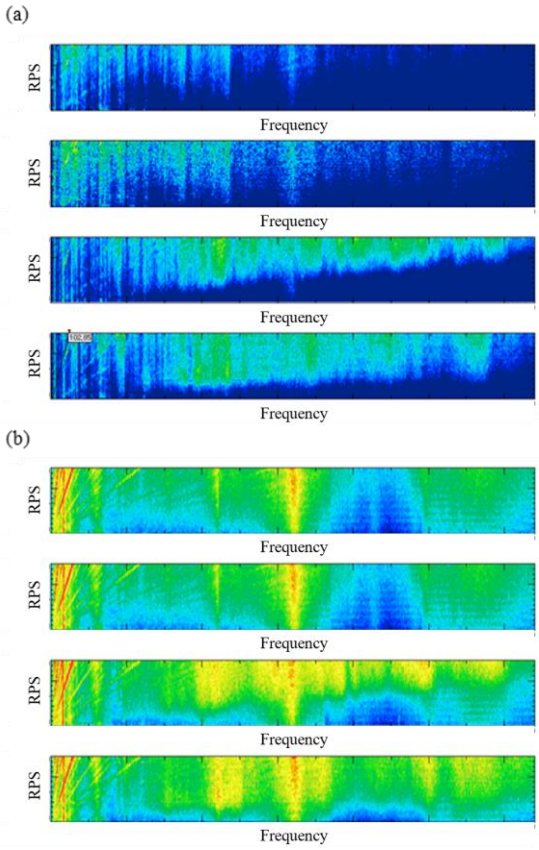

Figure 7. The C-EPS operation noise test (a) microphone, (b) accelerometer STFT results of 'Normal', interference noise type 'A', 'B', and 'C' (From top to bottom)

Figure 7. presents the STFT results of operational noise test for 'Normal', interference noise types 'A', 'B', and 'C'. Comparing to Figure 6, it can be observed that there are distinct visual differences in the FTFM regions where the model concentrates on classifying. To obtain better information of the noise sources in the FTFM regions, signal post-processing was conducted. The time signal data were bandpass filtered in the 4–6 kHz range, which was identified as the most distinguishing frequency band between 'Normal' and defective C-EPS in the FTFM. To analyze amplitude variations in the filtered time signal data, the Hilbert transform [18] was applied, and the envelope was calculated.

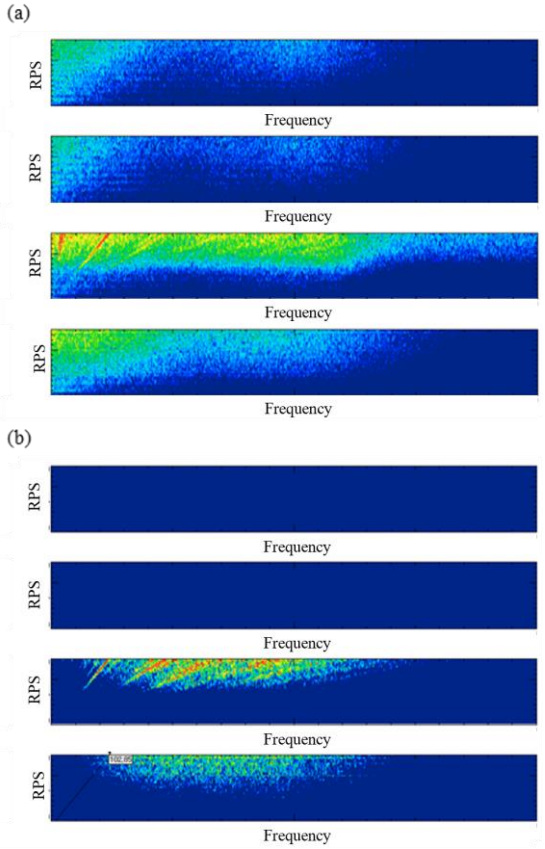

Figure 8. The C-EPS operation noise test (a) microphone, (b) accelerometer bandpass filtered Hilbert transformation envelope results of 'Normal', interference noise type 'A', 'B', and 'C' (From top to bottom)

As shown in Figure 8., In case of 'B' type interference noise, the bearing fault frequency are distinctly observed, unlike in the STFT results. This can be interpreted as the noise and acceleration signals generated by the bearing during interference noise occurrence being masked by motor and reduction gear signals, leading to information loss. After filtering, these signals were clearly distinguished. However, unlike the microphone, which captures bearing fault frequencies directly, the accelerometer data revealed sideband patterns around the reduction gear order. It can be observed that the signal amplitude is relatively low in low-speed steering conditions. This is because the filtering was

performed using a simple 4–6 kHz band-pass filter rather than the order pattern FTFM of interference noise 'B,' resulting in the inability to capture the characteristics of relatively lower frequency bands in low steering speed conditions. In case of 'C' type interference noise, it shows a wide frequency range without a diagonal pattern. These results correspond with human subjective evaluations, where interference noise 'B' exhibited perceptible periodic amplitude modulation, 'A' occurred intermittently, and 'C' was perceived as a harsh sound. The above results demonstrate that the FTFM incorporates real system's noise and vibration characteristics.

5. CONCLUSION

In this study, to improve the detection rate of defective C-EPS, a CNN model was trained on operation noise test data, and XAI techniques were used to extract the FTFM, which represents the frequency features by steering speed that the model focused on. When using FTFM, a higher defective C-EPS detection rate was observed compared to conventional methods. Additionally, further post-signal processing within the identified feature regions demonstrated that FTFM incorporate the noise and vibration characteristics of the system. Based on these results, the XAI-based C-EPS noise and vibration analysis method has been validated as effective. Furthermore, using FTFM enables the optimization of test methods, including the selection of steering speed intervals with high weights and relevant frequency bands, while also demonstrating the potential for estimation of noise sources. Although FTFM masking cannot superior than the defect detection rate of the deep learning model itself, it has the advantage of being directly applicable to existing EOL equipment. During this study, it was confirmed that various human errors, such as decreased concentration and adaptation to noise, occur. Focusing on these issues, the next study will conduct unsupervised learning using an autoencoder to compare its effectiveness with human labeling. it will also investigate whether the parts with increased reconstruction error in the STFT can be used like FTFM to improve defect detection rates and whether they contain information on the noise and vibration characteristics of interference noise, comparing these findings with XAI.

6. REFERENCES

[1] Kozaki, Y., Hirose, G., Sekiya, S., and Miyaura, Y. "Electric power steering (EPS)." *Motion and Control*, vol. 6, pp. 9-15, 1999.

[2] Tagawa, Yuki, Rytis Maskeliūnas, and Robertas Damaševičius. "Acoustic anomaly detection of mechanical failures in noisy real-life factory environments." *Electronics*, vol. 10, no. 19, pp. 2329, 2021.

[3] Marchi, Erik, Fabio Vesperini, Stefano Squartini, and Björn Schuller. "Deep recurrent neural network‐based autoencoders for acoustic novelty detection." *Computational Intelligence and Neuroscience*, vol. 2017, no. 1, pp. 4694860, 2017.

[4] Peng, Bo, Danlei Li, I. Kevin, Kai Wang, and Waleed H. Abdulla. "Acoustic-Based Industrial Diagnostics: A Scalable Noise-Robust Multiclass Framework for Anomaly Detection." *Processes*, vol. 13, no. 2, pp. 544, 2025.

[5] Duman, Taha Berkay, Barış Bayram, and Gökhan İnce. "Acoustic anomaly detection using convolutional autoencoders in industrial processes." in *Proc. of 14th International Conference on Soft Computing Models in Industrial and Environmental Applications (SOCO 2019)*, (Seville, Spain), pp. 432-442, 2020.

[6] Giovannardi, E., S. Delvecchio, N. Cavina, C. Colangeli, B. Cornelis, and K. Janssens. "Full vehicle NVH end-of-line testing and data-driven fault detection of a high-performance hybrid vehicle front e-axle."

[7] Nam, Gue-Hwan, Seok-Jun Bu, Na-Mu Park, Jae-Yong Seo, Hyeon-Cheol Jo, and Won-Tae Jeong. "Data augmentation using empirical mode decomposition on neural networks to classify impact noise in vehicle." In *ICASSP 2020-2020 IEEE International Conference on Acoustics, Speech and Signal Processing (ICASSP)*, pp. 731-735. IEEE, 2020.

[8] Blickensdorff, Johannes, Andrei Degtiarev, Kashaf Gulzar, Hans Fleischmann, and René Grünke. "Production Quality Testing for Automotive Electric Drive Units with AI-Enabled Anomaly Detection based on NVH Data." *DAGA*, 2023.

[9] Panza, Maria Antonietta. "A review of experimental techniques for NVH analysis on a commercial vehicle." *Energy Procedia*, vol. 82, pp. 1017-1023, 2015.

[10] Gonzalez, Patxi, Garikoitz Buigues, and Angel Javier Mazon. "Noise in electric motors: A comprehensive review." *Energies*, vol. 16, no. 14, pp. 5311, 2023.

[11] Tuma, Jiri. "Gearbox noise and vibration prediction and control." *International Journal of Acoustics and Vibration*, vol. 14, no. 2, pp. 99-108, 2009.

[12] McInerny, Sally A., and YJIToe Dai. "Basic vibration signal processing for bearing fault detection." *IEEE Transactions on Education*, vol. 46, no. 1, pp. 149-156, 2003.

[13] He, Kaiming, Xiangyu Zhang, Shaoqing Ren, and Jian Sun. "Deep residual learning for image recognition." In Proceedings of the *IEEE Conference on Computer Vision and Pattern Recognition*, pp. 770-778, 2016.

[14] Dosovitskiy, Alexey, Lucas Beyer, Alexander Kolesnikov, Dirk Weissenborn, Xiaohua Zhai, Thomas Unterthiner, Mostafa Dehghani et al. "An image is worth 16x16 words: Transformers for image recognition at scale." *arXiv preprint arXiv*:2010.11929, 2020.

[15] Selvaraju, Ramprasaath R., Michael Cogswell, Abhishek Das, Ramakrishna Vedantam, Devi Parikh, and Dhruv Batra. "Grad-cam: Visual explanations from deep networks via gradient-based localization." *In Proceedings of the IEEE International Conference on Computer Vision*, pp. 618-626, 2017.

[16] Ribeiro, Marco Tulio, Sameer Singh, and Carlos Guestrin. ""Why should I trust you?" Explaining the predictions of any classifier." *In Proceedings of the 22nd ACM SIGKDD International Conference on Knowledge Discovery and Data Mining*, pp. 1135-1144, 2016.

[17] Lundberg, Scott M., and Su-In Lee. "A unified approach to interpreting model predictions*." Advances in Neural Information Processing Systems*, vol. 30, 2017.

[18] Feldman, Michael. "Hilbert transform in vibration analysis." *Mechanical Systems and Signal Processing*, vol. 25, no. 3, pp. 735-802, 2011.